In cellulo FRET-FLIM and single molecule tracking reveal the supra-molecular organization of the pyoverdine bio-synthetic enzymes in *Pseudomonas aeruginosa*

Véronique Gasser[1,2,*], Morgane Malrieu[3,*], Anne Forster[1,2], Yves Mély[3],
Isabelle J. Schalk[1,2] and Julien Godet[3,4] ⓘ

[1]Université de Strasbourg, UMR7242, ESBS, Bld Sébastien Brant, F-67413 Illkirch, Strasbourg, France; [2]CNRS, UMR7242, ESBS, Bld Sébastien Brant, F-67413 Illkirch, Strasbourg, France; [3]Laboratoire de Bioimagerie et Pathologies, UMR CNRS 7021, Université de Strasbourg, Illkirch, France and [4]Groupe Méthode Recherche Clinique, Hôpitaux Universitaires de Strasbourg, France

Abstract

The bio-synthesis of pyoverdine (PVD) in *Pseudomonas aeruginosa* involves multiple enzymatic steps including the action of non-ribosomal peptide synthetases (NRPSs). One hallmark of NRPS is their ability to make usage of non-proteinogenic amino-acids synthesized by co-expressed accessory enzymes. It is generally proposed that different enzymes of a secondary metabolic pathway assemble into large supra-molecular complexes. However, evidence for the assembly of sequential enzymes in the cellular context is sparse. Here, we used *in cellulo* single-molecule tracking and Förster resonance energy transfer measured by fluorescence lifetime microscopy (FRET-FLIM) to explore the spatial partitioning of the ornithine hydroxylase PvdA and its interactions with NRPS. We found PvdA was mostly diffusing bound to large complexes in the cytoplasm with a small exchangeable trapped fraction. FRET-FLIM clearly showed that PvdA is physically interacting with PvdJ, PvdI, PvdL, and PvdD, the four NRPS involved in the PVD pathway in *Pseudomonas aeruginosa* PAO1. The binding modes of PvdA were strikingly different according to the NRPS it is interacting with, suggesting that PvdA binding sites have co-evolved with the enzymatic active sites of NRPS. Our data provide evidence for strongly organized multi-enzymatic complexes responsible for the bio-synthesis of PVD and illustrate how binding sites have evolved to finely control the co-localization of sequential enzymes and promote metabolic pathway efficiency.

CAMBRIDGE UNIVERSITY PRESS

Introduction

To improve fitness, bacteria have evolved sophisticated machinery to produce secondary metabolites with remarkable structural and functional diversities. Secondary metabolites are often produced by specific and dedicated bio-synthetic pathways activated in response to environmental stimuli. If much is understood about the enzymatic cascades and mechanisms that underlie these bio-syntheses, comparatively little is known about the cellular organization of their components (Meyer *et al.*, 2014). There is a long-standing hypothesis that enzymes involved in a metabolic pathway must organize into supra-molecular complexes (Schmitt and An 2017), so that secondary metabolite synthesis is orchestrated by the assembly of sequential enzymes. This process is expected to be widespread (Narayanaswamy *et al.*, 2009) (including in eukaryotic cells (An *et al.*, 2008; French *et al.*, 2016)) and to play an important role in the overall bio-synthesis efficiency or regulation (An *et al.*, 2008; Castellana *et al.*, 2014). However observations on such specific multi-protein organizations are sparse in the cellular context and most of them are resulting from microscopy co-localization observations (Schmitt and An 2017).

Here we used the pyoverdine (PVD) metabolic pathway of *Pseudomonas aeruginosa* PAO1 as a model system. PVDs are large fluorescent siderophores composed by an invariant (1S)-5-amino-2,3-dihydro-8,9-dihydroxy-1H-pyrimido(1,2-a)quinoline core grafted to a 6- to 12-amino acids chain (Meyer, 2000; Ravel and Cornelis, 2003). In PAO1, PVD synthesis relies on four non-ribosomal peptide synthetases (NRPSs); namely PvdL, PvdI, PvdJ, and PvdD (Georges and Meyer, 1995; Lehoux *et al.*, 2000; Mossialos *et al.*, 2002; Ackerley *et al.*, 2003; Lamont and Martin, 2003) (Fig. 1). NRPSs are large modular enzymes synthesizing peptides independently from ribosomes (Finking and Marahiel, 2004; Strieker *et al.*, 2010). Each NRPS module is responsible for the incorporation of a defined monomer into the final product (Strieker *et al.*, 2010) (Fig. 1*c*). The PVD precursor in PAO1 is an 11 amino-acid (AA) peptide with the sequence L-Glu–L-Tyr–D-Dab–L-Ser–L-Arg–L-Ser–L-fOHOrn–L-Lys–L-fOHOrn–L-Thr–L-Thr. The second and third amino acids of the peptide (L-Tyr and D-amino butyric
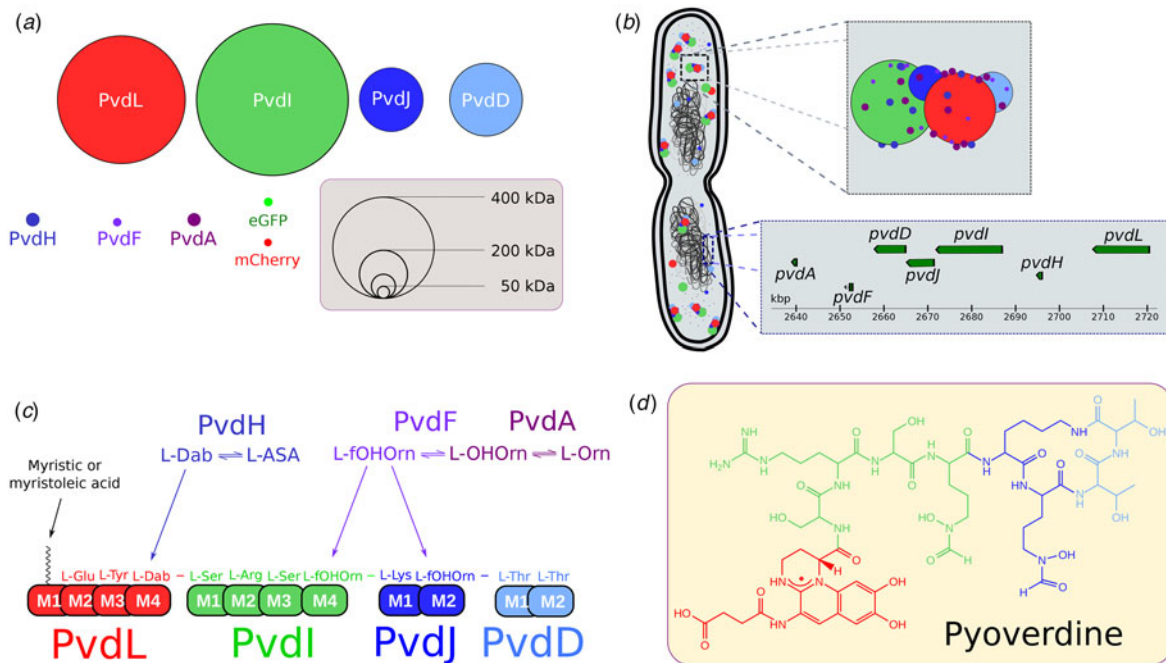
Fig. 1. NRPS of *P. aeruginosa* PAO1. (*a*) Enzymes involved in the cytoplasmic bio-synthesis of the PVD precursor in PAO1. Four large NRPSs (PvdL, PvdI, PvdJ, and PvdD) are responsible for the synthesis of an 11 amino-acid (AA) peptide and for the incorporation of modified AA, produced by PvdH(L-Dab) and by PvdA and PvdF (L-fOH Orn) accessory proteins. The diameters of the enzymes are proportional to their molecular weights. eGFP and mCherry are shown for MW comparison. (*b*) Schematic view of the chromosomic genes and cytoplasmic proteins involved in the early steps of the PVD bio-synthetic pathway in PAO1. Genes coding for NRPSs and accessory proteins are found in a large biosynthetic gene cluster (BGC). Once the PVD pathway is activated, proteins encoded by genes in the BGC are expressed and may organize in siderophore-specific multi-enzymatic complexes called siderosomes. (*c*) PVD precursor sequence. During bio-synthesis, each NRPS module is responsible for the incorporation of a defined AA. PvdL (red), PvdI (green), PvdJ (blue), and PvdD (light blue) are acting sequentially to add respectively 3,4,2 and 2 AA of the 11-AA sequence of the PVD precursor. (*d*) PVD (type I) – the major siderophore synthesized by PAO1 – is the maturated form of the cytoplasmic precursor of 11 AA.

acid) will form the chromophore in the PVD mature form. The use of non-proteinogenic amino acids, including D-isomers, is the hallmark of NRPS and is responsible for the sequence diversity of non-ribosomal peptides and derived products (Marahiel *et al.*, 1997). Accessory and tailoring enzymes are required to synthesize modified amino-acids assembled by NRPS into the final peptide. In PAO1, PvdA (Visca *et al.*, 1994), PvdF (McMorran *et al.*, 2001), and PvdH (Ikai and Yamamoto, 1997; Lamont and Martin, 2003) are involved in the synthesis of L-fOHOrn and D-Dab. Their genes are found at proximity of NRPS genes in PAO1 genome (Fig. 1*b*) in large bio-synthetic gene clusters (BGCs) (Chiang *et al.*, 2011; Gulick, 2017). These cytoplasmic enzymes are thus likely co-expressed with NRPS when the PVD pathway is activated.

PvdA catalyzes the FAD-dependent hydroxylation of the amine side chain of ornithine using nicotinamide adenine dinucleotide phosphate (NADPH) as the electron donor and molecular oxygen to synthesize N5-hydroxy-ornithine (Ge and Seah, 2006; Meneely *et al.*, 2009). Recent fluorescence microscopy findings have shown a high cellular organization of PVD-related proteins with clusters of PvdA co-localizing with PvdD, PvdL, and PvdJ in fluorescence microscopy (Guillon *et al.*, 2012; Imperi and Visca, 2013). Pull-down assays using a recombinant hexa histidine-tagged PvdA protein as a bait captured low amount of PvdJ and PvdL (Imperi and Visca, 2013). PvdA has also been shown to interact with PvdJ M2 isolated module in yeast double-hybrid experiments (Imperi and Visca, 2013). Taken together, these data suggest that PvdA is interacting with NRPS and may be part of large multi-enzymatic complexes named siderosomes (Guillon *et al.*, 2012; Imperi and Visca, 2013; Gasser *et al.*, 2015). However a clear bio-chemical characterization of these complexes is missing – possibly

due to highly dynamic interactions between the proteins of the siderosomes and/or their transient formation (Gasser *et al.*, 2015). Moreover only a few attempts for characterizing these complexes in the cellular environment have been reported. In this context, *in cellulo* characterization with high temporal and/or spatial resolution is required to capture siderosomes organization.

In this work, we investigated the localization and dynamics of PvdA in cells using single-particle tracking combined with single-molecule tracking localization using photo-activated localization microscopy (sptPALM (Manley *et al.*, 2008)). The statistical description of thousands of single PvdA traces in cells showed that PvdA was mostly diffusing as large complexes in the cytoplasm, except for a small restricted and exchangeable fraction diffusing with a lower diffusion rate. We additionally used Förster resonance energy transfer (FRET) measured by fluorescence lifetime imaging microscopy (FLIM (Bastiaens and Squire, 1999)) to evidence PvdA interactions with PvdJ, PvdI, PvdL, and PvdD. Although the exact determination of the complex stoichiometry was not accessible from FLIM-FRET measurements, our data are consistent with transient interactions of several PvdA on PvdI, PvdD, and PvdL whereas PvdJ interacts with PvdA in a 1 : 1 stoichiometry. Our data evidence a complex organization of siderosomes and suggest that PvdA binding sites have co-evolved with NRPS module specificity.

Materials and methods

Bacterial strains, plasmids, and growth conditions

P. aeruginosa strains used in this study are listed in Supplementary Table S1. Bacteria were grown in 5 mL lysogeny

broth (Difco) at 30 °C under 220 rpm orbital shaking. To induce the expression of the PVD pathway enzymes, *P. aeruginosa* strains were pelleted by centrifugation, washed, and further grown overnight at 30 °C in an iron-deficient succinate medium (composition: 6 g L^{-1} K$_2$HPO$_4$, 3 g L^{-1} KH$_2$PO$_4$, 1 g L^{-1} (NH$_4$)$_2$SO$_4$, 0.2 g L^{-1} MgSO$_4$, 7H$_2$O, and 4 g L^{-1} sodium succinate with the pH adjusted to 7.0 by adding NaOH). Cells were finally diluted and grown an additional 24 h. The presence of PVD in the supernatant can be visually observed as an intense yellow-green water-soluble pigment.

Mutants construction

All enzymes for deoxyribonucleic acid (DNA) manipulation were purchased from ThermoFisher Scientific and were used in accordance with the manufacturer's instructions. *E. coli* strain TOP10 (Invitrogen) was used as the host strain for all plasmids. The DNA fragments from *P. aeruginosa* used for cloning were amplified from the genomic DNA of the PAO1 strain with Phusion High-Fidelity DNA polymerase (ThermoFisher Scientific). The primers used are listed in supplementary Table S3 of the Supporting Information. As previously described (Guillon *et al.*, 2012), the general procedure for the construction of the plasmids involved insertion of the mcherry, egfp or photo-activatable mcherry gene flanked by upstream and downstream regions of 700 bp, corresponding to the insertion site, into a pME3088 or a pEXG2 vector. For the pVEGA30 plasmid, pEXG2 was amplified by the primers pEXG2HindIIIR and pEXG2EcoRIF, and the egfp gene flanked by upstream and downstream regions of 700 bp ligated into the plasmid by blunt-end cloning. Mutations in the chromosomal genome of *P. aeruginosa* were generated by transferring the suicide vector from *E. coli* TOP10 strain into the *P. aeruginosa* recipient strain and allowing the plasmid to integrate into the chromosome, with selection for tetracycline resistance for pME3088 (Voisard *et al.*, 1994) or gentamicin resistance for pEXG2. A second crossing-over event excising the vector was achieved by enrichment for tetracycline-sensitive cells (pME3088) or sucrose resistant cells selection (pEXG2), to generate the corresponding mutants (Ye *et al.*, 1995). All tag insertion mutants were verified by PCR and sequencing.

Wide field imaging

Wide field imaging was performed on a Micro-Manager (Edelstein *et al.*, 2014) controlled Olympus IX-81 inverted microscope equipped with z-drift control and an auto-focus system (ZDC Olympus). Phase images were generated using a Phase3 100× 1.4NA objective (Olympus) using a 512 × 512 pixels EM-CCD (ImagEM – Hamamatsu Photonics – Japan). Epifluorescence excitation was provided by a 488 nm laser diode (spectra physics) using a 488 nm (Di01-R488 – Semrock) dichroic filter. Fluorescence signals were filtered using a 488 nm long pass filter (BLP01-488R-25 – Semrock). Live-cells were immobilized on a 1% agarose pad and imaged at 20 °C. Quantitative fluorescence measurements were performed at the cell level using a home-made imageJ plugin for cell segmentation and fluorescence quantification. Initial cell segmentation was based on a Laplacian of Gaussian (LoG) filtering of the phase image and further used to define a rod-shape contour (sphero-cylinder) based on different central moment calculations. Initial rod-shape contours were then refined based on the isotropic 3 × 3 gradient of the initial image to adjust bacteria contours.

Photo-activated localization microscopy (PALM) and single particle tracking-PALM (sptPALM)

PALM and sptPALM (Manley *et al.*, 2008) were performed on a home-built Micro-Manager (Edelstein *et al.*, 2014) controlled inverted-microscope based on a Nikon Eclipse II equipped with a 100× 1.49 objective (Nikon – Japan) and a drift focus compensator (Perfect Focus System – Nikon – Japan). Photo-activable mCherry (PA-mCherry) was excited with a 561 nm diode laser (Oxxius – France) and activated with a 405 nm laser diode (Spectra Physics – Germany) selected by an acousto-optic tunable filter (AOTFnC 400-650 TN, AA Otpo Electronic- France). Fluorescence emission of PA-mCherry was collected through a quadri-band dichroic filter (FF405/496/560/651-Di01-25 × 36 – Semrock – USA) and further filtered with a 561 nm long-pass filter (561 nm RazorEdge, Semrock – France). The wavefront distortions of the emission signal were corrected using an adaptive optics device (MicAO, Imaging Optics – France) before being imaged on a 512 × 512 pixels EM-CCD (ImagEM – Hamamatsu Photonics – Japan) operating at −65 °C with an ADU to photon conversion factor of about 60. Image stacks ranging from 2000 to 5000 frames with an exposure time of 16 to 50 ms were typically recorded for sptPALM using a home-written Beanshell acquisition script. Molecule localizations were retrieved using Peakfit, an open source software package for Fiji and further analyzed using self-written script in R. Tracking traces were generated using the simple Linear Assignment Problem (LAP) tracker (Jaqaman *et al.*, 2008) implemented in TrackMate plugin (Tinevez *et al.*, 2017) for Fiji. The simple LAP is well suited for tracking molecules undergoing Brownian motion or for low density of molecules undergoing non-Brownian motion. Data were further analyzed in R according to a jump distance analysis (Weimann *et al.*, 2013) assuming the mean square displacement is proportional to the two-dimensional diffusion coefficient D (in 2-D Brownian motion) such that $\langle r^2(\Delta t) \rangle = 4D_j \times \Delta t$. Diffusion coefficients were retrieved from the empirical cumulative distribution function (ecdf) of the particles' displacements in a set time interval according to:

$$P(r^2, \Delta t) = 1 - \sum_{j=1}^{m} f_j \times e^{-\frac{r^2}{4D_j \times \Delta t}}$$

The choice the ecdf rather than the discrete probability density function (pdf) histogram for fitting was motivated by the dependence of the pdf histogram to the user input for bin-size selection – possibly biasing the fitting parameters.

Hidden Markov model (HMM) estimates were obtained using the Baum–Welch algorithm (Baum *et al.*, 1970) and the Viterbi algorithm (Viterbi, 1967), both implemented in the R HMM package (https://cran.r-project.org/package=HMM) that predict the most likely sequence of Markov states given the observed dataset. Diffusion coefficients were obtained from the HMM exponential rates. HMM parameter confidence intervals (exponential rates and transition matrix) were obtained by bootstrap.

The tracking analysis procedure was challenged using data of the Particle Tracking Challenge (http://www.bioimageanalysis.org/track/) found in Supplementary Video 1 of reference (Chenouard *et al.*, 2014) corresponding to simulated images of vesicles undergoing Brownian motions with a medium particle density and a signal-to-noise ratio of four. Retrieved parameters were in excellent agreement with the ground truth as shown in Supplementary Fig. S5.

Fluorescence lifetime imaging microscopy (FLIM)

Time-correlated single-photon counting FLIM measurements were performed on a home-made two-photon excitation scanning microscope based on an Olympus IX70 inverted microscope with an Olympus 60×1.2 NA water immersion objective operating in de-scanned fluorescence collection mode (Batisse *et al.*, 2013; El-Meshri *et al.*, 2015). Two-photon excitation at 930 nm was provided by a Ti:Sapphire oscillator (Mai Tai® DeepSee™, Spectra Physics – 80 MHz repetition rate, ≈70 fs pulse width) at 10–20 mW. Fluorescence photons were collected through a 680 nm short pass filter (F75-680, AHF, Germany) and a 525/50 nm band-pass filter (F37-516, AHF, Germany) and directed to a fiber-coupled avalanche photo-diode (SPCM-AQR-14-FC, Perkin Elmer) connected to a time-correlated single photon counting module (SPC830, Becker & Hickl, Germany). Cells grown for 48 h in succinate media were immobilized on a 1% agarose pad and rapidly imaged. Typically, area of 50×50 μm in the samples was scanned at 4 μs per pixel (1024×1024 pixels) for 100 to 600 s to reach the Nyquist–Shannon sampling criteria and to achieve the appropriate photon statistics to investigate the fluorescence decays. Fluorescence decays were processed using a commercial software package (SPCImage V2.8, Becker & Hickl, Germany). A binning of two was applied before processing the fluorescence decays. FLIM data were further analyzed using a homemade ImageJ plugin and R scripts as described in reference (Godet and Mely, 2019).

Results

PvdA diffuses within large complexes in the cytoplasm

To localize PvdA enzyme in its intracellular environment, we produced strains expressing at the chromosomal level PvdA fused to eGFP, eYFP or PAmCherry at its C-terminus as previously described (Guillon *et al.*, 2012; Gasser *et al.*, 2015). These strains genetically expressed fluorescent PvdA at physiological levels as shown by quantitative reverse transcription PCR (RT-qPCR) (Guillon *et al.*, 2012; Gasser *et al.*, 2016). The expression of fluorescent PvdA was increased in iron-deprived growing conditions. These strains were able to produce PVD (see Supplementary Fig. S1). Epifluorescence microscopy showed that PvdA-eGFP was localized in the cytoplasm. The level of expression of PvdA-eGFP was heterogeneous from cell to cell. No spatial organization was observed along the cell cycle, except for some unilateral polar spots in few cells (Fig. 2a and b). However, the resolution of epifluorescence microscopy is too low to rule out sub-diffraction limit (∼250 nm) organizations. To explore more in detail the localization and diffusion of single PvdA in live cells, we used photoactivated localization microscopy (PALM) – a single molecule localization microscopy method allowing to determine the position of individual fluorescent molecules with nanometer accuracy in live cells (Betzig *et al.*, 2006). In PALM, tiny fractions of PvdA-PAmCherry are photo-activated at each acquisition frame, allowing determining their localizations with sub-diffraction precision. Thousands of sparse subsets of molecule coordinates pinpointed sequentially in time can then be accumulated within an imaged area. Using TIRF illumination limiting the observation, the cytoplasmic zone immediately above the membrane contacting the surface, PvdA-PAmCherry was found to localize homogeneously in the cytoplasm. Despite a retrieved density of 2000–3000 molecule localizations per μm², high enough to define spatial arrangements at a resolution of ∼40 nm resolution,

no particular structural organization was observed for PvdA, with the exception of preferential accumulation at one pole in some cells (Guillon *et al.*, 2012). We also used PALM to perform high-density sptPALM to explore PvdA molecular trajectories within the cell. About 6000 individual trajectories were computed from ∼54 000 linkable individual localizations in 42 cells, allowing the construction of single molecule diffusion maps at the single cell level. Diffusion patterns appeared very similar from cell to cell (Fig. 2b), with traces of heterogeneous velocities scattered throughout the cytoplasm (Fig. 2c). We were not able to identify exclusion areas. To take advantage of the large number of short trajectories obtained with PvdA-PAmCherry in live cells, we computed jump-distances (JDs) defined as the distance travelled by a single molecule during a fixed time lag Δt (from 16 to 50 ms). Over the population of molecules, JD distribution reflects the fine features of the underlying diffusion mechanisms and/or the number of diffusing species (Fig. 2d) (Weimann *et al.*, 2013). JD histograms of PvdA were found very similar to the different cells. Assuming PvdA underwent Brownian motions, a nice adjustment of the empirical cumulative distribution of the JD was obtained with a two-populations model (Fig. 2e), suggesting the presence of two diffusing populations of PvdA. Diffusion coefficients were 0.06 (0.02; 0.08) and 0.47 (0.39–0.54) μm² s⁻¹. We assigned these values to trapped and diffusing species, respectively (Fig. 2f). Due to the finite localization precision (localization error of ∼30–40 nm), PvdA molecules diffusing at 0.06 μm² s⁻¹ could indiscriminately correspond to trapped, restrained or immobile fractions and were therefore referred as restrained hereafter. This fraction was found to represent about 10 to 24% (median 15%) of the total tracked PvdA. The value of 0.47 (0.39–0.54) μm² s⁻¹ is about one order of magnitude slower as compared to the observed or calculated diffusion of free cytoplasmic proteins with the same molecular weight in *E. coli* (Kalwarczyk *et al.*, 2012). Although the viscosity of the cytoplasm of PAO1 might be slightly increased due to its smaller volume and its larger genome size as compared to *E. coli*, it is unlikely to explain such a difference. PvdA must therefore diffuse in the cytoplasm bound to a large complex.

To explore possible transitions between these two populations, we adjusted the square of the displacement values with a discrete two-state HMMs assuming an exponential probability distribution. The HMM provides information about the average duration time in a state before transition, the probabilities for molecules to transition from one state to the other and the mean diffusion value of each state. A representative tracking trace (although much longer than the 128 ms median trace duration) is presented in Fig. 2g for illustration, together with its cumulative square displacement (CSD) plotted over time (Chung *et al.*, 2010) (Fig. 2h) to provide a visual representation of the HMM model output. An overall linear increase of CSD for a given time window indicates that the JDs are distributed around their average value and therefore that the molecule diffuses uniformly. Break points defined by changes in slopes are likely to correspond to state transitions. It is clearly illustrated in Fig. 2g and h that the HMM model properly identifies the two states and their transitions. The transition probability matrix Pi of the model is presented in Fig. 2i. A PvdA in the restrained state has a probability of about 9% to transition to the mobile fraction on the next frame whereas only about 2% of the mobile PvdA are expected to become restrained. Although the probabilities are low, about 260 events of mobile-to-restrained and restrained-to-mobile transitions were observed within traces showing the two diffusion regimen are
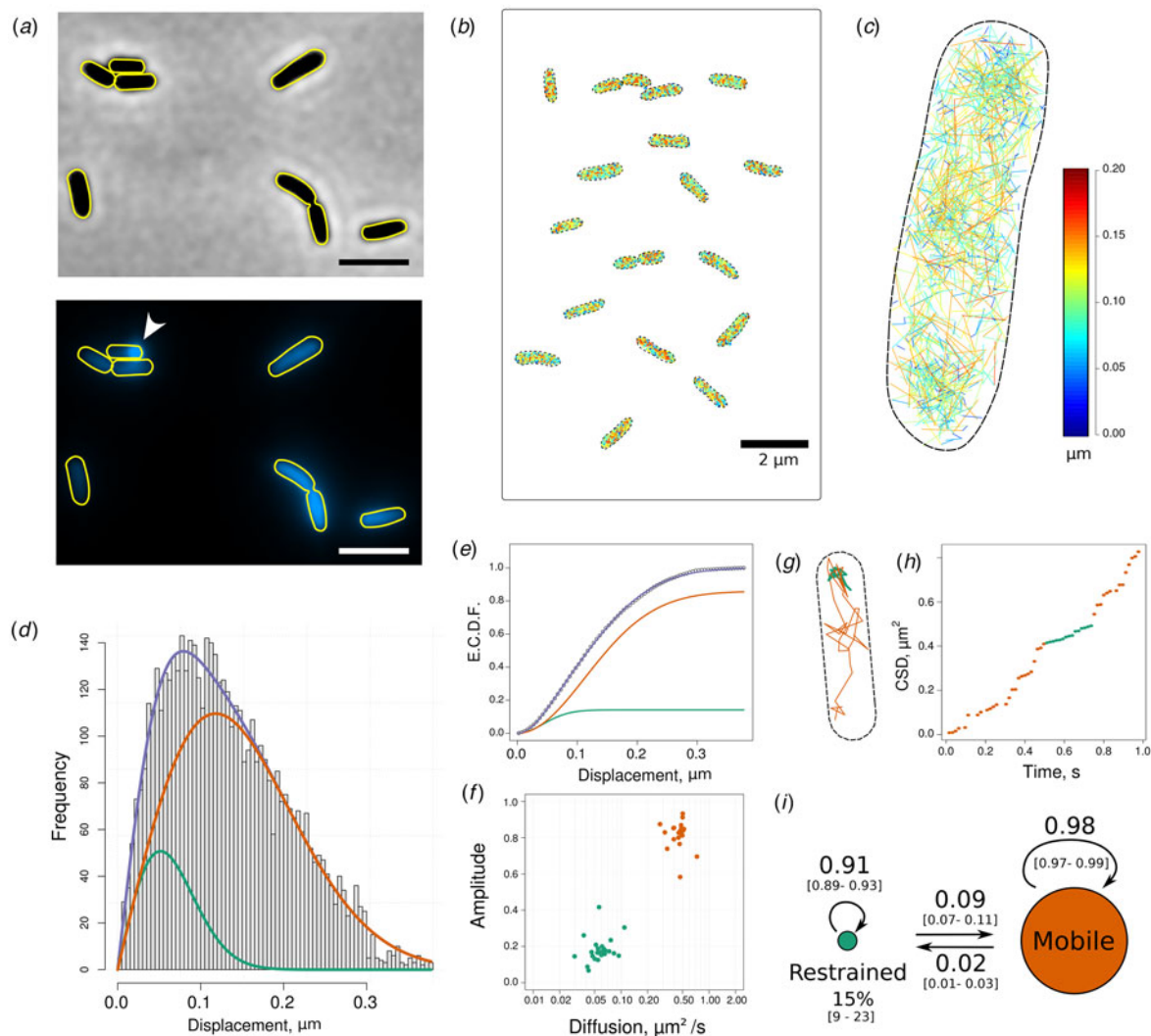
Fig. 2. Single molecule tracking of PvdA-PAmCherry in live *P. aeruginosa* PAO1. (*a*) Phase-contrast (upper) and fluorescence (lower) images of PvdA-eGFP in PAO1 grown in succinate media at 30 °C for 48 h. PvdA-eGFP is found homogeneously distributed in the cytoplasm. Some cells presented fluorescent spots at one pole (white arrow), as previously described (Guillon *et al.*, 2012; Imperi and Visca, 2013; Gasser *et al.*, 2015). Scale bars = 2 µm. (*b*) Concatenated image of representative PvdA-PAmCherry cell diffusion maps obtained by sptPALM at 20 °C and (*c*) magnification of a representative single cell diffusion map. Trajectories steps are color-coded to indicate instantaneous jump distances (JDs) (µm observed during Δt = 16 ms time interval). (*d*) JD distribution representing the Euclidean distances travelled by ∼23 800 PvdA-PAmCherry molecules during a 16 ms time interval. These data correspond to the JD observed in 29 cells measured in four independent experiments. (*e*) The corresponding ecdf was fitted assuming a two-population diffusion model. Diffusion coefficients of 0.06 (0.02–0.08) µm² s⁻¹ and 0.47 (0.39–0.54) µm² s⁻¹ [median (IQR)] were determined for the restrained (green) and mobile (orange) complexes, respectively. (*f*) Scatter plot of the amplitude of the restrained and mobile forms of PvdA-PAmCherry as a function of their corresponding diffusion coefficients (*n* = 23 cells). (*g*) Single PvdA-PAmCherry tracking trace observed at 62.5 Hz and (*h*) its cumulative square distance (CSD) as a function of time. The trace and the CSD are color-encoded according to their diffusion regime defined by a discrete two-state HMMs. (*i*) Schematic representation of the probability transition matrix retrieved from the HMM. The diameters of the diffusion regimen are proportional to their steady-state amplitudes. The probability of transition from mobile to restrained regimen was 2%. The bootstrapped 2.5 and 97.5% percentiles of the transition matrix parameters are in squared brackets.

exchangeable. Finally, the amplitudes of the two populations were calculated as the steady-state probability distribution of the stationary Markov chain. A value of 15% [$\mathrm{CI}_{95\%} = (9;23)\%$] was associated with the constrained state, in very good agreement with the estimation made by fitting the JD empirical cumulative distribution. All these results were reproduced using PvdA-eYFP to rule out any quantification artefacts possibly resulting from PAmCherry photo-physical properties (see Supplementary Fig. S2).

Taken together, these data clearly demonstrate that PvdA was mostly diffusing in the cytoplasm bound to large protein complexes without evidence for any spatial organization pattern nor cytoplasmic exclusion areas at a ∼40 nm resolution (TIRF illumination). A small fraction estimated at ∼15% exhibited a reduced diffusion rate. We assigned it to trapped complexes. The diffusing and trapped complexes were found exchangeable.

PvdI interacts with many PvdA

PvdA is an ornithine hydroxylase (Meneely *et al.*, 2009) working in tandem with the hydroxy-ornithine transformylase PvdF (McMorran *et al.*, 2001) to generate fOH-Ornithine used as a building block by PvdI and PvdJ. To explore whether NRPSs are cytoplasmic partners of PvdA, we sought to explore the

physical interactions between PvdA and PvdI in live cells producing PVD. We used FLIM to measure FRET. FLIM is a general technique to probe changes in fluorophores' local environment. In time-domain FLIM, a pulsed laser periodically excites the fluorophores in the sample. Following excitation, fluorophores relax into their ground-state either by emitting a photon (radiative decay) or through a non-radiative pathway. The fluorescence lifetime τ is defined as the average time a fluorophore remains in the excited state after excitation according to:

$$\tau = \frac{1}{k_r + k_{nr}}$$

in which k_r and k_{nr} are the radiative and the non-radiative rate constants, respectively.

Experimentally, each detected fluorescence photon is tagged with its arrival time relative to the last excitation laser pulse. The fluorescence lifetime τ can thus be retrieved by adjusting the experimental fluorescence decay with a sum of exponentials defined by rates inversely proportional to their fluorescence lifetimes. In the presence of a fluorescence acceptor (as mCherry) in the close vicinity of a fluorescence donor (as eGFP), FRET can occur – increasing the non-radiative de-excitation rate k_{nr} of the donor and thus decreasing its fluorescence lifetime. FRET can only occur if the acceptor is only a few apart from the donor, a distance range implying physical interaction between the labeled molecules. FLIM FRET is therefore particularly well suited to probe protein–protein interactions in living cells (Bastiaens and Squire, 1999; Day *et al.*, 2001; Sengupta and Lippincott-Schwartz, 2012). Moreover, as the fluorescence lifetime is an intrinsic parameter of the fluorophore independent of concentration, FRET-FLIM is more robust than intensity-based methods to measure FRET when concentrations of interacting partners cannot be controlled.

Strains expressing only PvdA-eGFP or PvdI-eGFP cultured in succinate media for 48 h were imaged using FLIM (Fig. 3a). Their fluorescence decays were adjusted with a single exponential model to retrieve their average fluorescence lifetime. The expression level of PvdA-eGFP, measured by the fluorescence intensity of cells on the microscopy images, was higher than that of PvdI-eGFP (see also Supplementary Fig. S3). But the fluorescence lifetime values of PvdA-eGFP or PvdI-eGFP were very similar with a median value of about 2.25 ns (Fig. 3b and c).

Co-expression of PvdI-mCherry with PvdA-eGFP resulted in a limited shortening of the average lifetime of PvdA-eGFP (Fig. 3b and c), suggesting poor interaction or long inter-dyes distances. In sharp contrast, the average lifetime of cells expressing PvdI-eGFP was significantly shortened in the presence of PvdA-mCherry. Energy transfer between PvdI-eGFP and PvdA-mCherry can be evidenced by comparing the lifetime distributions of PAO1 expressing PvdI-eGFP *versus* PvdI-eGFP PvdA-mCherry (Fig. 3b) or by comparing their corresponding empirical cumulative distributions (Fig. 3d). FRET can also be evidenced by comparing the lifetimes averaged by cells (Fig. 3c). It seems unlikely that the mere exchange of eGFP for mCherry or mCherry for eGFP has such a dramatic effect on PvdA/PvdI interaction. Indeed, both strains retain the ability of producing PVD with similar efficiencies (although lower than that of the wild-type PAO1 (see Supplementary Fig. S1)). The apparent contradiction in the above findings can be reconciled if we consider the expression levels of the two proteins with an expression of PvdA-eGFP far

higher than that of PvdI-eGFP (see Supplementary Fig. S3). It can then be envisioned that PvdA-eGFP used as a donor coexists as a minor fraction transferring energy to mCherry and a major fraction free of transfer, both forms exhibiting different fluorescence lifetimes. Because the time resolved fluorescence decay sums photons emitted by the different species, the resulting fluorescence decay of PvdA-eGFP–PvdI-mCherry will thus tend towards the decay of PvdA-eGFP as the relative amount of non-transferring PvdA-eGFP increases. In contrast, the fluorescence decay of cells co-expressing PvdI-eGFP and PvdA-mCherry will be shifted to lower lifetimes, as the less abundant PvdI-eGFP protein is transferring to the nearby PvdA-mCherry. To take this species mixture into account, fluorescence decays were fitted with a two-exponential component model in which the average lifetime is defined as a weighted sum of two decays according to:

$$\langle \tau \rangle = \sum_{i=1}^{2} \alpha_i \times \tau_i$$

To limit over-fitting and improve fitting convergence, the long-lived lifetime τ_2 was fixed at the 90th percentile of PvdA-eGFP or PvdI-eGFP lifetimes defined using a single exponential decay (2.25–2.30 ns), whereas the lifetime value of the fast decay τ_1 and the relative contribution of each component defined by α_1 and α_2 could float. For a two-component model $\alpha_2 = 1 - \alpha_1$ and $\langle \tau \rangle$ can thus be rewritten as:

$$\langle \tau \rangle = \tau_2 - \alpha_1 \times (\tau_2 - \tau_1)$$

A successful fit procedure will converge toward $\langle \tau \rangle$ by adjusting τ_1 and α_1 and will provide τ_1 and α_1 conditional probability distributions given the fixed τ_2 value. A plot of τ_1 as a function of α_1 can be drawn as a diagram to represent observations made over all fitted pixels. An estimation of the 2D density of the pixel spatial distribution in this plot provides an estimation of the average lifetime (center of the density map contour plot) but also the bivariate distribution of (τ_1, α_1) parameters. The distribution of (τ_1, α_1) measurements of PvdI-eGFP PvdA-mCherry was scattered with a significant part of the distribution showing shortened τ_1 as compared to PvdI-eGFP lifetime – with values ranging from about 2.2 ns down to 1.6 ns (Fig. 3e). This confirmed a pronounced energy transfer between the two fluorophores. The fraction of pixel decays better adjusted with a single exponential was only about 5% (Fig. 3e inset). These FLIM data clearly showed that PvdA is physically interacting with PvdI.

In sharp contrast, the distribution of (τ_1, α_1) parameters of PvdA-eGFP–PvdI-mCherry was mostly positioned in an area corresponding to an average lifetime of about 2.2 ns with τ_1 values about 2.1 ns (Fig. 3f). If an equimolar complex of PvdA and PvdI was formed, the two (τ_1, α_1) maps for PvdI-eFGP–PvdA-mCherry and PvdA-eGFP–PvdI-mCherry should look very similar, only being shifted along the α_1 axis due to the difference in the relative amount of energy transferring species. Indeed, if we consider the difference in the expression level of the two enzymes, almost all the PvdI molecules should be bound to PvdA (high value for α_1) while only a small fraction of PvdA should be bound to PvdI (low value of α_1) but in both cases τ_1 should not be affected because the structure of the interacting complex should remain the same. Our observations largely
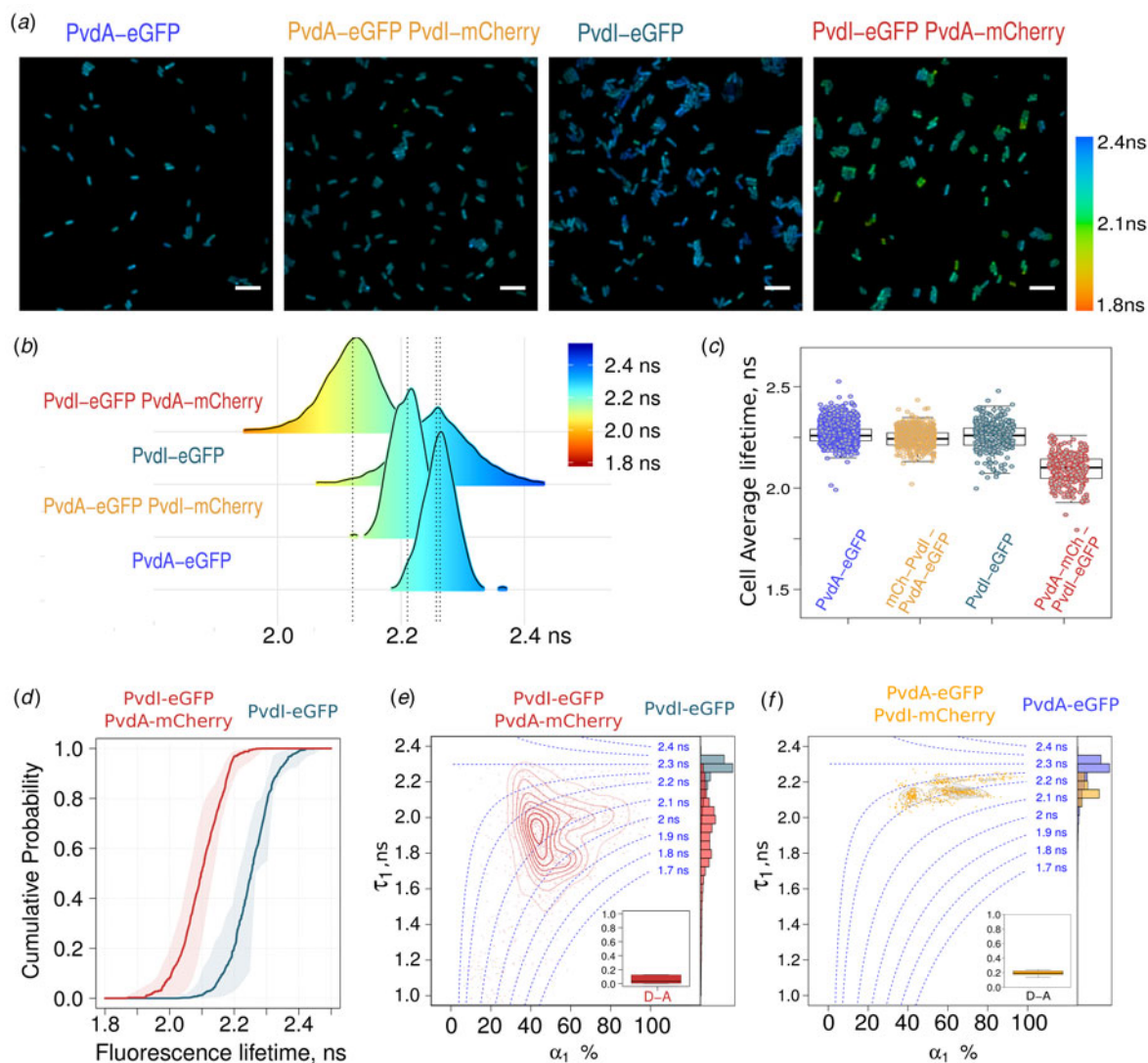
Fig. 3. FRET-FLIM measurement of the PvdA–PvdI interaction in live PAO1. (*a*) Representative FLIM images of (from left to right) PvdA-eGFP, PvdA-eGFP PvdI-mCherry, PvdI-eGFP, and PvdI-eGFP PvdA-mCherry strains showing limited shortening in the average lifetime of PvdA-eGFP co-expressed with PvdI-mCherry in PAO1 but a larger effect for PvdI-eGFP co-expressed with PvdA-mCherry. All images are color-encoded according to the pixel fluorescence lifetime values. The same color scale (on the right) is used for the four images. Scale bar = 5 µm. (*b*) Probability density distribution of the mean fluorescence lifetime of pixels of (from bottom to top) PvdA-eGFP (*n* = 10 863), PvdA-eGFP PvdI-mCherry (*n* = 13 127), PvdI-eGFP (*n* = 6962), and PvdI-eGFP PvdA-mCherry (*n* = 14 456) strains from at least *N* = 3 independent experiments (*n* = number of pixels). (*c*) Average fluorescence lifetime of individual cells of (from left to right) PvdA-eGFP (n_{cell} = 1154; *N* = 8), PvdA-eGFP PvdI-mCherry (n_{cell} = 486; *N* = 3), PvdI-eGFP (n_{cell} = 291; *N* = 3), and PvdI-eGFP PvdA-mCherry (n_{cell} = 303; *N* = 3) (n_{cell} = number of analyzed cells; *N* = number of independent experiments). (*d*) Empirical cumulative probability distribution of the fluorescence lifetime of PvdI-eGFP and PvdI-eGFP PvdA-mCherry (data from panel B). (*a*), (*b*), (*c*), and (*d*) provide evidence for a physical interaction between PvdA and PvdI. (*e*) and (*f*) Density map with contour lines of (τ_1, α_1) fitting parameters showing clusters of pixels with similar decay signature for (*e*) PvdI-eGFP PvdA-mCherry (red) and (*f*) PvdA-eGFP PvdI-mCherry (orange). The histograms of the short-lived lifetime (τ_1) of the donor–acceptor couple and the average lifetime⟨τ⟩of the corresponding donor-only conditions are plotted as marginal histograms. Inset: box plot of the fraction per cell of pixels better fitted with a single exponential decay model – corresponding to decays with no energy transfer.

differed from this situation with τ_1 values being also affected. This difference is likely explained by the presence of multiple acceptors, further shortening the average lifetime according to:

$$\langle \tau \rangle = \left(1/\tau_D + \sum_{i=1}^{n} k_i \right)^{-1}$$

in which *n* is the number of acceptors and k_i and τ_D, the rate of energy transfer and the donor lifetime, respectively. The short τ_1 values observed for PvdI-eGFP PvdA-mCherry (compare red contour lines in Fig. 3*e* and orange ones in Fig. 3*f*) are likely

explained by the presence of the complexes of several PvdA-mCherry surrounding PvdI-eGFP in a range of distances compatible with FRET. One can thus infer that multiple PvdA-mCherry proteins are bound per PvdI-eGFP NRPS.

Taken together, these observations provide evidence for a physical interaction between PvdA and PvdI and suggest that multiple PvdA are bound to one molecule of PvdI.

PvdA interacts with PvdJ

As PvdJ also contains a module responsible for the addition of L-fOH-Ornithine in the PVD peptide, we decided to monitor
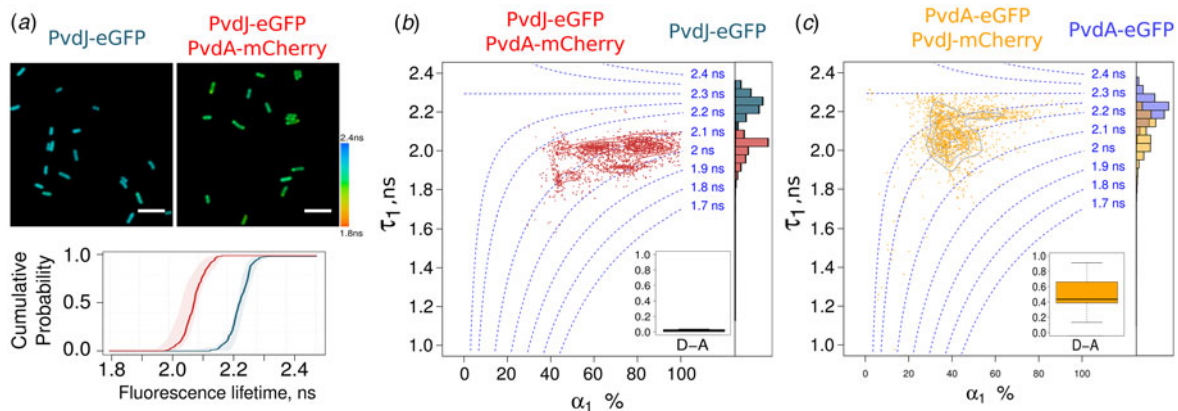
Fig. 4. FRET-FLIM measurement of the PvdA–PvdJ interaction in live PAO1. (*a*) Representative FLIM images of PvdJ-eGFP and PvdJ-eGFP PvdA-mCherry strains. Using a single exponential analysis, a shortening of the lifetime of PvdJ-eGFP co-expressed with PvdA-mCherry is observed in live PAO1. The cumulative probability of the fluorescence lifetime of these two strains demonstrates the interaction of PvdA with PvdJ in live cells. (*b*) Density map with contour lines of (τ_1, α_1) fitting parameters of PvdJ-eGFP (grey) and PvdJ-eGFP PvdA-mCherry (red). (*c*) Density map with contour lines of (τ_1, α_1) fitting parameters of PvdA-eGFP (blue) and PvdA-eGFP PvdJ-mCherry (orange). (*b*) and (*c*) provide evidence for a major and possibly unique binding site for PvdA on PvdJ.

FLIM-FRET between PvdA and PvdJ (Fig. 4*a*). The lifetime of PvdJ-eGFP PvdA-mCherry estimated from a single exponential decay model was shortened by about 10–15% (2.0–2.1 ns) as compared to the PvdJ-eGFP fluorescence lifetime (Fig. 4*a*). As for PvdA–PvdI interaction, we could not define any preferential area where the interaction takes place. Using a two-exponential decay model, the fraction of decays better adjusted with a single exponential model was close to zero (Fig. 4*b* inset). The distribution of τ_1 was centered at about 2.0 ns and the amplitude of the short-lived component was representing about 60 to 80%. Interestingly, a similar τ_1 value was observed for the fraction of PvdA-eGFP molecules interacting with PvdJ-mCherry but associated with a α_1 value of ~40%. Therefore, the same τ_1 value observed for the both labeling schemes of the two enzymes. This strongly suggests the presence of a unique complex with a well-defined binding site for PvdA on PvdJ that governs the interaction. This conclusion is in line with a previous report showing by double-hybrid experiment that PvdA interacts with PvdJ M2 isolated module (Imperi and Visca, 2013) – the module responsible for incorporation of formyl-OHOrn (Fig. 1*c*). The high value of α_1 observed for PvdJ-eGFP PvdA-mCherry indicated that in the cellular context, the PvdA binding site of PvdJ is saturated with the ornithine hydroxylase. Unfortunately, we cannot infer from our data if it corresponds to a site with strong affinity and a long residence time of PvdA on PvdJ or to a situation of fast exchange of PvdA molecules on this binding site.

PvdA interacts with PvdL and PvdD in cells

We further investigated the interaction of PvdA with PvdL (Fig. 5*a*–*c*) and PvdD (Fig. 5*d*–*f*). None of these two NRPSs are using PvdA product as a building block. We were nevertheless able to evidence physical interactions between PvdA and PvdL (Fig. 5*a*–*c*) and between PvdA and PvdD (Fig. 5*d*–*e*). It clearly appeared that the binding mode of PvdA to PvdL differed from the binding of PvdA to PvdD. It was also visible that results observed for PvdL (Fig. 5*a*–*c*) were very similar to that observed for PvdI (Fig. 3*d*–*f*). On the other hand, observations made for PvdD (Fig. 5*d*–*f*) were broadly like PvdJ (Fig. 4*a*–*c*) with a significant amount of interacting eGFP-PvdD characterized by a τ_1 value of about 2.0 ns – the same τ_1 value than that measured

for the small fraction of PvdA-eGFP interacting with mCherry-PvdD Fig. 5*f*. But in contrast to PvdJ, a second binding site with a shorter τ_1 value (about 1.8 ns) was also present (Fig. 5*e*) – suggesting that PvdD can accommodate more than one PvdA protein.

Discussion

In this work, we constructed PAO1 strains with modified genes coding for PvdA and NRPS fluorescent proteins (see Supplementary Table S1) inserted at the chromosomal level. These tagged enzymes retained the expression levels and functions of the endogenous ones (Gasser *et al.*, 2016). We used these strains to explore interactions between PvdA and the four NRPS responsible for the bio-synthesis of the PVD peptide backbone. We found that PvdA was not existing as a free protein in the cytoplasm but was engaged in large complexes. We inferred from FLIM data the physical interactions of PvdA with PvdI and PvdJ but also with PvdL and PvdD and demonstrated different binding modes of PvdA on the different NRPSs.

Based on the differences in FRET distributions between strains expressing PvdA tagged with the fluorescent donor (PvdA-eGFP) as compared to strains expressing PvdA tagged with the acceptor mCherry, we evidenced the simultaneous binding of multiple PvdA bound to several NRPSs and clearly distinguished this situation from complexes with 1:1 stoichiometry. Interestingly, the interaction of PvdA with PvdI and with PvdJ, the two NRPSs using fOHOrn as a building block, differed in extent and nature. The presence of several binding sites has to be considered to explain our FLIM observations with PvdI. The interaction of several PvdA with PvdI may fulfill the need for an excess of substrate locally available to optimize the activity of the PvdI enzyme. An unbalanced binding stoichiometry may also compensate fOHOrn dilution in the cell cytoplasm. On the contrary, a major binding site for PvdA was found on PvdJ. The M2 module previously identified by two-hybrid as an interacting partner of PvdA (Imperi and Visca, 2013) and responsible for fOHOrn insertion is a good candidate to harbor this binding site for PvdA. The difference in binding mechanism of the two NRPSs is striking if we consider that both PvdI and PvdJ require the action of PvdA. Since PvdL exhibits a global binding behavior
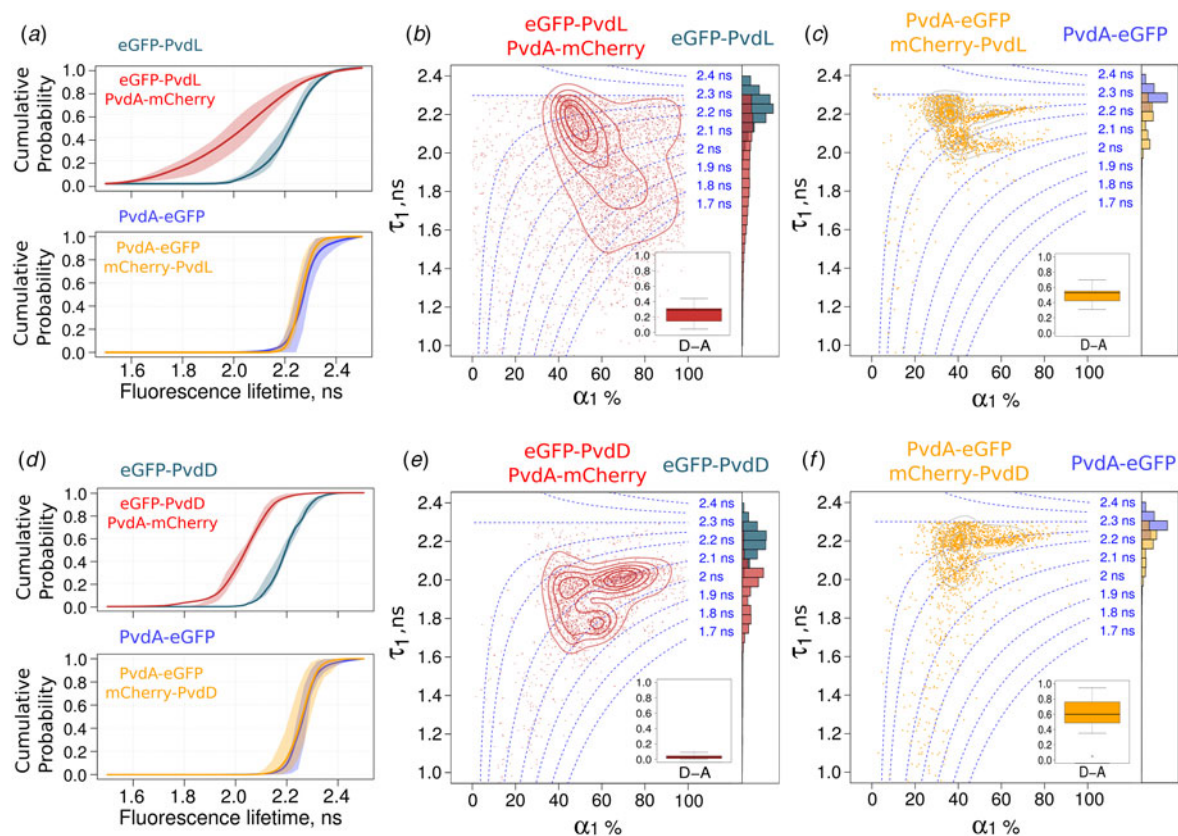
Fig. 5. FRET-FLIM measurement of the PvdA–PvdL and PvdA–PvdD interactions in live PAO1. Cumulative probability of the fluorescence lifetime of the PvdA–PvdL (a) and PvdA–PvdD complexes (d). Larger fluorescence lifetime decrease was observed when PvdL or PvdD was labelled with eGFP. Density map with contour lines of (τ_1, α_1) fitting parameters of (in B) eGFP-PvdL (grey) and eGFP-PvdL PvdA-mCherry (red) and (in C) PvdA-eGFP (blue) and PvdA-eGFP mCherry-PvdL (orange). Density map with contour lines of (τ_1, α_1) fitting parameters of (in e) eGFP-PvdD (grey) and eGFP-PvdD PvdA-mCherry (red) and (in f) PvdA-eGFP (blue) and PvdA-eGFP mCherry-PvdD (orange).

very similar to PvdI, the molecular size of the NRPS could be an element explaining the binding mode – the larger the NRPS the higher the number of PvdA binding sites the enzyme can accommodate. Additional speculations can be made. For instance, a connection could be made between (i) the conserved position of fOH-Orn in the PVD sequence of *Pseudomonas aeruginosa* and (ii) the presence or not of a single or multiple binding sites. PVD production is a characteristic of the fluorescent pseudomonads. But *Pseudomonas* species produce slightly different PVDs. *P. aeruginosa* strains are able to produce three different PVDs, PVD I, PVD II and PVD III with a different peptide sequences. Amongst the PVD sequences of *P. aeruginosa*, the module 2 of PvdJ is well conserved and the fOHOrn is highly conserved at that position 9 in the PVD precursor sequence. On the contrary, the position where the fOHOrn is inserted by PvdI in the PVD precursor is more variable and corresponds either to module 2, 3 or 4 of PvdI in the different *P. aeruginosa* strains (Kilz *et al.*, 1999; Meyer, 2000). In this context, evolving multiple binding sites outside the modules provides the necessary flexibility to ensure that the product produced by PvdA is available whatever the fOH ornithine module position within PvdI. It suggests additionally that rather than physical coordination between active sites of tailoring enzymes and NRPS modules, only co-localization of sequential enzymes seems to be enough to promote metabolic efficiency. Taken together, we can then envisage binding sites have co-evolved with module specificity.

Although we did not interrogate direct interactions between the different NRPS in this work, our findings provide strong evidence for siderosomes. Such organization has been previously hypothesized based on biochemical observations, but the difficulty to handle these complexes limits their explorations *in vitro*. The reversibility of spatial assemblies of sequential metabolic enzymes – proposed as a general mechanism to regulate metabolic activities – may explain why their *in-vitro* study remains extremely challenging. Our data demonstrate the possibility to capture rich information on protein–protein interactions which allows to directly characterize siderosomes in the cellular environment even if their formation is transient. This type of observation is susceptible to provide valuable data regarding the importance of maintaining effective protein–protein interactions in recombinant NRPS templates (Brown *et al.*, 2018), or more generally recombinant metabolic machinery. But our work also raised some questions in particular regarding the slow diffusion of PvdA and the fraction with restrained diffusion. Does it correspond to complexes interacting with PvdE, the transporter responsible for the PVD precursor exports to the periplasm (Yeterian *et al.*, 2010)? Are siderosomes interacting with the inner membrane and can they therefore be considered as metabolons? In both cases, the exploration of the possible additional regulation resulting from specific spatial partitioning within the bacterial cytoplasm will require three-dimensional multi-color explorations in the cellular context.

Taken together, our data clearly evidence that secondary metabolite pathways are much more organized than initially envisioned, with multiple interactions and multiple binding modes between accessory proteins and NRPSs. If clustering of all the PVD bio-synthesis machinery in a single complex is possibly increasing the synthesis efficiency, notably by sequestring intermediate products, the understanding of how metabolic enzymes interact and coordinate with each other in space and time to ensure their metabolic functions is mostly at its infancy. But due to their non-vital nature and their experimentally tractable expression, siderosomes are good candidates to be used as model systems to demonstrate the functional significance of highly orchestrated enzyme organizations in the cellular context. Additional general knowledge gained from siderosome will likely contribute further to the general understanding of mechanisms ruling widespread metabolic pathways and cellular organizations.

References

Ackerley DF, Caradoc-Davies TT and Lamont IL (2003) Substrate specificity of the nonribosomal peptide synthetase PvdD from *Pseudomonas aeruginosa. Journal of Bacteriology* **185**, 2848–2855.

An S, Kumar R, Sheets ED and Benkovic SJ (2008) Reversible compartmentalization of de novo purine biosynthetic complexes in living cells. *Science (New York, N.Y.)* **320**, 103–106. https://doi.org/10.1126/science.1152241.

Bastiaens PI and Squire A (1999) Fluorescence lifetime imaging microscopy: spatial resolution of biochemical processes in the cell. *Trends in Cell Biology* **9**, 48–52.

Batisse J, Guerrero SX, Bernacchi S, Richert L, Godet J, Goldschmidt V, Mély Y, Marquet R, de Rocquigny H and Paillart J-C (2013) APOBEC3G impairs the multimerization of the HIV-1 vif protein in living cells. *Journal of Virology* **87**, 6492–6506.

Baum LE, Petrie T, Soules G and Weiss N (1970) A maximization technique occurring in the statistical analysis of probabilistic functions of Markov chains. *Annals of Mathematical Statistics* **41**, 164–171.

Betzig E, Patterson GH, Sougrat R, Wolf Lindwasser O, Olenych S, Bonifacino JS, Davidson MW, Lippincott-Schwartz J and Hess HF (2006) Imaging intracellular fluorescent proteins at nanometer resolution. *Science (New York, N.Y.)* **313**, 1642–1645.

Brown AS, Calcott MJ, Owen JG and Ackerley DF (2018) Structural, functional and evolutionary perspectives on effective re-engineering of nonribosomal peptide synthetase assembly lines. *Natural Product Reports* **35**, 1210–1228.

Castellana M, Wilson MZ, Xu Y, Joshi P, Cristea IM, Rabinowitz JD, Gitai Z and Wingreen NS (2014) Enzyme clustering accelerates processing of intermediates through metabolic channeling. *Nature Biotechnology* **32**, 1011–1018.

Chenouard N, Smal I, de Chaumont F, Maška M, Sbalzarini IF, Gong Y, Cardinale J, Carthel C, Coraluppi S, Winter M, Cohen AR, Godinez WJ, Rohr K, Kalaidzidis Y, Liang L, Duncan J, Shen H, Xu Y, Magnusson KEG, Jaldén J, Blau HM, Paul-Gilloteaux P,

Roudot P, Kervrann C, Waharte F, Tinevez JY, Shorte SL, Willemse J, Celler K, van Wezel JP, Dan HW, Tsai YS, Ortiz de Solórzano C, Olivo-Marin JC and Meijering E (2014) Objective comparison of particle tracking methods. *Nature Methods* **11**, 281–289.

Chiang Y-M, Chang S-L, Oakley BR and Wang CCC (2011) Recent advances in awakening silent biosynthetic gene clusters and linking orphan clusters to natural products in microorganisms. *Current Opinion in Chemical Biology* **15**, 137–143.

Chung I, Akita R, Vandlen R, Toomre D, Schlessinger J and Mellman I (2010) Spatial control of EGF receptor activation by reversible dimerization on living cells. *Nature* **464**, 783–787.

Day RN, Periasamy A and Schaufele F (2001) Fluorescence resonance energy transfer microscopy of localized protein interactions in the living cell nucleus. *Methods (San Diego, Calif.)* **25**, 4–18.

Edelstein AD, Tsuchida MA, Amodaj N, Pinkard H, Vale RD and Stuurman N (2014) Advanced methods of microscope control using Manager software. *Journal of Biological Methods* **1**, 10.

El-Meshri SE, Dujardin D, Godet J, Richert L, Boudier C, Darlix JL, Didier P, Mély Y and de Rocquigny H (2015) Role of the nucleocapsid domain in HIV-1 gag oligomerization and trafficking to the plasma membrane: a fluorescence lifetime imaging microscopy investigation. *Journal of Molecular Biology* **427**, 1480–1494.

Finking R and Marahiel MA (2004) Biosynthesis of nonribosomal peptides 1. *Annual Review of Microbiology* **58**, 453–488.

French JB, Jones SA, Deng H, Pedley AM, Kim D, Chan CY, Hu H, Pugh RJ, Zhao H, Zhang Y, Huang TJ, Fang Y, Zhuang X, Benkovic SJ (2016) Spatial colocalization and functional link of purinosomes with mitochondria. *Science (New York, N.Y.)* **351**, 733–737.

Gasser V, Guillon L, Cunrath O and Schalk IJ (2015) Cellular organization of siderophore biosynthesis in *Pseudomonas aeruginosa*: evidence for siderosomes. *Journal of Inorganic Biochemistry* **148**, 27–34.

Gasser V, Baco E, Cunrath O, August PS, Perraud Q, Zill N, Schleberger C, Schmidt A, Paulen A, Bumann D, Mislin GL, Schalk IJ (2016) Catechol siderophores repress the pyochelin pathway and activate the enterobactin pathway in *Pseudomonas aeruginosa*: an opportunity for siderophore-antibiotic conjugates development. *Environmental Microbiology* **18(3)**, 819–832. https://doi.org/10.1111/1462-2920.13199.

Ge L and Seah SYK. 2006. Heterologous expression, purification, and characterization of an l-ornithine N(5)-hydroxylase involved in pyoverdine siderophore biosynthesis in *Pseudomonas aeruginosa. Journal of Bacteriology* **188**, 7205–7210.

Georges C and Meyer JM (1995) High-molecular-mass, iron-repressed cytoplasmic proteins in fluorescent pseudomonas: potential peptide-synthetases for pyoverdine biosynthesis. *FEMS Microbiology Letters* **132**, 9–15.

Godet J and Mely Y (2019) Exploring protein-protein interactions with large differences in protein expression levels using FLIM-FRET. *Methods and Applications in Fluorescence* **8(1)**, 014007. https://doi.org/10.1088/2050-6120/ab5dd2.

Guillon L, Mecherki ME, Altenburger S, Graumann PL and Schalk IJ (2012) High cellular organization of pyoverdine biosynthesis in *Pseudomonas aeruginosa*: clustering of PvdA at the old cell pole. *Environmental Microbiology* **14**, 1982–1994.

Gulick AM (2017) Nonribosomal peptide synthetase biosynthetic clusters of ESKAPE pathogens. *Natural Product Reports* **34**, 981–1009.

Ikai H and Yamamoto S (1997) Identification and analysis of a gene encoding L-2,4-diaminobutyrate:2-ketoglutarate 4-aminotransferase involved in the 1,3-diaminopropane production pathway in *Acinetobacter baumannii. Journal of Bacteriology* **179** : 5118–5125.

Imperi F and Visca P (2013) Subcellular localization of the pyoverdine biogenesis machinery of *Pseudomonas aeruginosa*: a membrane-associated 'siderosome'. *FEBS Letters* **587**, 3387–3391.

Jaqaman K, Loerke D, Mettlen M, Kuwata H, Grinstein S, Schmid SL and Danuser G (2008) Robust single-particle tracking in live-cell time-lapse sequences. *Nature Methods* **5**, 695–702.

Kalwarczyk T, Tabaka M and Holyst R (2012) Biologistics—diffusion coefficients for complete proteome of *Escherichia coli. Bioinformatics (Oxford, England)* **28**, 2971–2978.

Kilz S, Lenz C, Fuchs R and Budzikiewicz H (1999) A fast screening method for the identification of siderophores from fluorescent *Pseudomonas* spp. by

liquid chromatography/electrospray mass spectrometry. *Journal of Mass Spectrometry* **34**, 281–290.

Lamont IL and Martin LW (2003) Identification and characterization of novel pyoverdine synthesis genes in *Pseudomonas aeruginosa*. *Microbiology (Reading,* England) **149**, 833–842.

Lehoux DE, Sanschagrin F and Levesque RC (2000) Genomics of the 35-Kb Pvd locus and analysis of novel PvdIJK genes implicated in pyoverdine biosynthesis in *Pseudomonas aeruginosa*. *FEMS Microbiology Letters* **190**, 141–146.

Manley S, Gillette JM, Patterson GH, Shroff H, Hess HF, Betzig E and Lippincott-Schwartz J (2008) High-density mapping of single-molecule trajectories with photoactivated localization microscopy. *Nature Methods* **5**, 155–157.

Marahiel MA, Stachelhaus T and Mootz HD (1997) Modular peptide synthetases involved in nonribosomal peptide synthesis. *Chemical Reviews* **97**, 2651–2674.

McMorran BJ, Shanta Kumara HM, Sullivan K and Lamont IL (2001) Involvement of a transformylase enzyme in siderophore synthesis in *Pseudomonas aeruginosa*. *Microbiology (Reading, England)* **147**, 1517–1524.

Meneely KM, Barr EW, Martin Bollinger J and Lamb AL (2009) Kinetic mechanism of ornithine hydroxylase (PvdA) from *Pseudomonas aeruginosa*: substrate triggering of O_2 addition but not flavin reduction. *Biochemistry* **48**, 4371–4376.

Meyer JM (2000) Pyoverdines: pigments, siderophores and potential taxonomic markers of fluorescent *Pseudomonas* species. *Archives of Microbiology* **174**, 135–142.

Meyer P, Cecchi G and Stolovitzky G (2014) Spatial localization of the first and last enzymes effectively connects active metabolic pathways in bacteria. *BMC Systems Biology* **8**, 131.

Mossialos D, Ochsner U, Baysse C, Chablain P, Pirnay J-P, Koedam N, Budzikiewicz H, Fernández DU, Schäfer M, Ravel J, Cornelis P (2002) Identification of new, conserved, non-ribosomal peptide synthetases from fluorescent pseudomonads involved in the biosynthesis of the siderophore pyoverdine. *Molecular Microbiology* **45**, 1673–1685.

Narayanaswamy R, Levy M, Tsechansky M, Stovall GM, O'Connell JD, Mirrielees J, Ellington AD and Marcotte EM (2009) Widespread reorganization of metabolic enzymes into reversible assemblies upon nutrient starvation. *Proceedings of the National Academy of Sciences of the United States of America* **106**, 10147–10152.

Ravel J and Cornelis P (2003) Genomics of pyoverdine-mediated iron uptake in pseudomonads. *Trends in Microbiology* **11**, 195–200.

Schmitt DL and An S (2017) Spatial organization of metabolic enzyme complexes in cells. *Biochemistry* **56**, 3184–3196.

Sengupta P and Lippincott-Schwartz J (2012) Quantitative analysis of photoactivated localization microscopy (PALM) datasets using pair-correlation analysis. *BioEssays: News and Reviews in Molecular, Cellular and Developmental Biology* **34**, 396–405.

Strieker M, Tanović A and Marahiel MA (2010) Nonribosomal peptide synthetases: structures and dynamics. *Current Opinion in Structural Biology* **20**, 234–240.

Tinevez J-Y, Perry N, Schindelin J, Hoopes GM, Reynolds GD, Laplantine E, Bednarek SY, Shorte SL and Eliceiri KW (2017) Trackmate: an open and extensible platform for single-particle tracking. *Methods (San Diego, Calif.)* **115**, 80–90.

Visca P, Ciervo A and Orsi N (1994) Cloning and nucleotide sequence of the PvdA gene encoding the pyoverdin biosynthetic enzyme L-ornithine N5-oxygenase in *Pseudomonas aeruginosa*. *Journal of Bacteriology* **176**, 1128–1140.

Viterbi A (1967) Error bounds for convolutional codes and an asymptotically optimum decoding algorithm. *IEEE Transactions on Information Theory* **13**, 260–269.

Voisard C, Bull CT, Keel C, Laville J, Maurhofer M, Schnider U, Dfago G and Haas D (1994) Biocontrol of root diseases by pseudomonas fluorescens CHA0: current concepts and experimental approaches. In O'Gara F, Dowling DN and Boesten B (eds), *Molecular Ecology of Rhizosphere Microorganisms*. Weinheim, Germany: Wiley-VCH Verlag GmbH, Book, pp. 67–89.

Weimann L, Ganzinger KA, McColl J, Irvine KL, Davis SJ, Gay NJ, Bryant CE and Klenerman D (2013) A quantitative comparison of single-dye tracking analysis tools using Monte Carlo simulations. *PloS One* **8**, e64287.

Ye RW, Haas D, Ka JO, Krishnapillai V, Zimmermann A, Baird C and Tiedje JM (1995) Anaerobic activation of the entire denitrification pathway in *Pseudomonas aeruginosa* requires Anr, an analog of Fnr. *Journal of Bacteriology* **177**, 3606–3609.

Yeterian E, Martin LW, Guillon L, Journet L, Lamont IL and Schalk IJ (2010) Synthesis of the siderophore pyoverdine in *Pseudomonas aeruginosa* involves a periplasmic maturation. *Amino Acids* **38**, 1447–1459.